AGU PUBLICATIONS

JGR

Journal of Geophysical Research: Solid Earth

RESEARCH ARTICLE
10.1002/2015JB012755

Key Points:
- A 3-D density model of the upper mantle is obtained for the Middle East and surrounding regions
- The results constrain the principal factors controlling the upper mantle heterogeneity
- The obtained density variations are directly related to the ongoing tectonic processes

Correspondence to:
M. K. Kaban,
kaban@gfz-potsdam.de

Citation:
Kaban, M. K., S. El Khrepy, N. Al-Arifi, M. Tesauro, and W. Stolk (2016), Three-dimensional density model of the upper mantle in the Middle East: Interaction of diverse tectonic processes, *J. Geophys. Res. Solid Earth*, *121*, 5349–5364, doi:10.1002/2015JB012755.

Received 9 NOV 2015
Accepted 5 JUN 2016
Accepted article online 7 JUN 2016
Published online 15 JUL 2016

Three-dimensional density model of the upper mantle in the Middle East: Interaction of diverse tectonic processes

Mikhail K. Kaban[1], Sami El Khrepy[2,3], Nassir Al-Arifi[2], Magdala Tesauro[4], and Ward Stolk[4]

[1]Helmholtz Centre Potsdam GFZ German Research Centre for Geoscience, Section 1.3: Earth System Modeling, Potsdam, Germany, [2]Vice Rectorate for Graduate Studies and Scientific Research, King Saud University, Riyadh, Saudi Arabia, [3]National Research Institute of Astronomy and Geophysics, Helwan, Egypt, [4]Department of Earth Sciences, University of Utrecht, Utrecht, Netherlands

Abstract We present a three-dimensional density model of the lithosphere and upper mantle for the Middle East and surroundings based on seismic, gravity, and seismic tomography data and analyze the main factors responsible for the density variations. The gravity effect of the crust is calculated and removed from the observed field using the most recent crustal model. The residual gravity anomalies are jointly inverted with the residual topography to image the density distribution within the upper mantle. The inversion is constrained by an initial density model based on seismic tomography. The obtained density variations span in a large range (±60 kg/m^3), revealing strong asymmetry in the density structure of the Arabian plate. The uppermost mantle layer in the Arabian Shield is relatively dense. However, below a depth of ~100 km we observe a strong low-density anomaly. In contrast, the mantle density in the Arabian platform increases at the same depths. The most pronounced decrease of the mantle density occurs in the Gulf of Aden, Red Sea, and East African Rift. Underneath the northern Red Sea the low-density anomaly is limited to the depth ~150 km, while in the southern part it is likely linked to a mantle plume. The densest mantle material is found under the South Caspian basin, which is likely associated with an eclogite body in the uppermost mantle. In the collision zones (the Zagros Belt and the Hellenic Arc), the high-density lithosphere shows the location of the subducting plates.

1. Introduction

The Middle East is characterized by active tectonics. Interaction of different tectonic processes results in a very complex structure, a high level of seismicity and continuous earthquake activity (Figure 1). An extension regime dominates the south-southwestern part of the region (the Gulf of Aden and the Red Sea); while on the northeast it is bounded by collisional zones (e.g., Zagros Mountains). Located in the center of the Middle East, the Arabian plate was formed by rifting of NE Africa from Arabia along the Red Sea and Gulf of Aden [*Stern and Johnson*, 2010]. The Arabian plate is relatively stable; although it is characterized by a strong heterogeneity likely related to the upper mantle structure [*Chen et al*., 2015]. Compressional and extensional forces acting on the opposite sides of the Arabian plate cause significant intraplate stresses [*Dewey and Şengör*, 1979]. The collision between the Arabian plate and Eurasia in the north and northeast leads to an intracontinental subduction and formation of the Anatolian-Iranian plateau and Zagros Mountains [e.g., *Stern and Johnson*, 2010]. Further to the north, the collision zone extends to the Caucasus region including also the Black and Caspian Sea. The Dead Sea fault system bounds the northwestern part of the Arabian plate and represents a north-south, left-lateral strike shear zone [*Smit et al*., 2010; *Agrawal et al*., 2015].

Mantle density heterogeneities, in particularly in the upper mantle, are closely related to tectonic processes. First of all, density contrasts produce significant stresses, which directly affect style and amplitude of lithospheric deformations [e.g., *Kaban et al*., 2015a]. Furthermore, continuous plate interactions and mantle underplating processes lead to accumulation of various anomalies (compositional, structural, and thermal) within the lithosphere. Seismic tomography does not always provide complete information about this heterogeneity. Therefore, knowledge of the mantle density structure is the key to understanding the tectonic processes and their surface expression. In the present study we integrate various data sets (e.g., gravity, geophysical, and geological data on the crustal structure, seismic tomography, and mineral physics), aiming to construct a 3-D density model of the upper mantle in the Middle East and surrounding regions and analyze this model with respect to the ongoing tectonic processes.

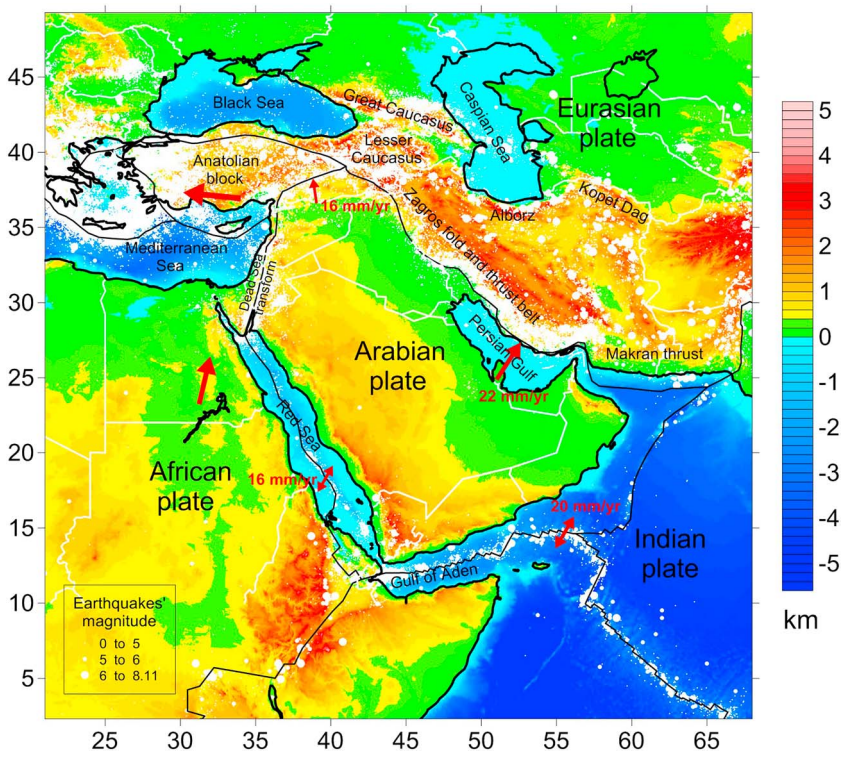

Figure 1. Location of study area (topography). Thin lines show the main plate boundaries. White circles show epicenters of earthquakes (ISC-GEM) [*Storchak et al.*, 2013]. Approximate plate velocity vectors are shown in red [*Stern and Johnson*, 2010].

To investigate the upper mantle density structure, it is necessary to reduce beforehand the impact of the crust, which completely hides the effect of the upper mantle density variations. Therefore, construction of a trustworthy three-dimensional density model of the crust, based on independent data (primarily seismic), is a prerequisite for density modeling of the upper mantle [*Kaban et al.*, 2010]. Fortunately, the crustal structure in many parts of the globe has been investigated by various geophysical methods, primarily seismic. Therefore, the effect of the crust can be calculated and removed from the observed fields in advance. Previous gravity studies of the Middle East were limited by the lack of data [*Seber et al.*, 2001]. Gravity field models had significant gaps because the existing terrestrial observations are very irregular and data from various gravity surveys are often inconsistent [e.g., *Kaban and Yuanda*, 2014]. Data on the crustal structure were also sparse [*Seber et al.*, 2001]. Presently, geophysical studies of the Middle East are undergoing revolution. New satellite data make it possible to create high-resolution gravity maps for the entire Earth [*Förste et al.*, 2014]. Furthermore, nearly all available seismic data have been recently integrated into a 3-D crustal model for most of Asia and the Middle East [*Stolk et al.*, 2013]. This information provides a robust input for the gravity modeling of the upper mantle in the region.

In the present study we investigate a three-dimensional density structure of the upper mantle in the Middle East and surrounding region. In the first stage the crustal effect is removed from the Bouguer gravity anomalies and topography. Furthermore, the effect of deep heterogeneity of the Earth is reduced using recent global dynamic models [*Kaban and Trubitsyn*, 2012; *Petrunin et al.*, 2013]. The calculated residuals reflect the effect of the upper mantle density variations. We construct an initial density model of the upper mantle based on a recent global seismic tomography model by *Schaeffer and Lebedev* [2013]. Finally, we employ an Occam's type inversion of the residual gravity anomalies and residual topography to calculate corrections for the initial model. In section 6, we discuss the constructed density model with respect to the tectonic structure of the Middle East.

2. Initial Data

2.1. Gravity Field

A new gravity field model EIGEN-6c4 [*Förste et al.*, 2014] is used in this study (Figure 2). In the continental area, this model combines data from recent satellite missions (chiefly GRACE and GOCE) and high-resolution terrestrial

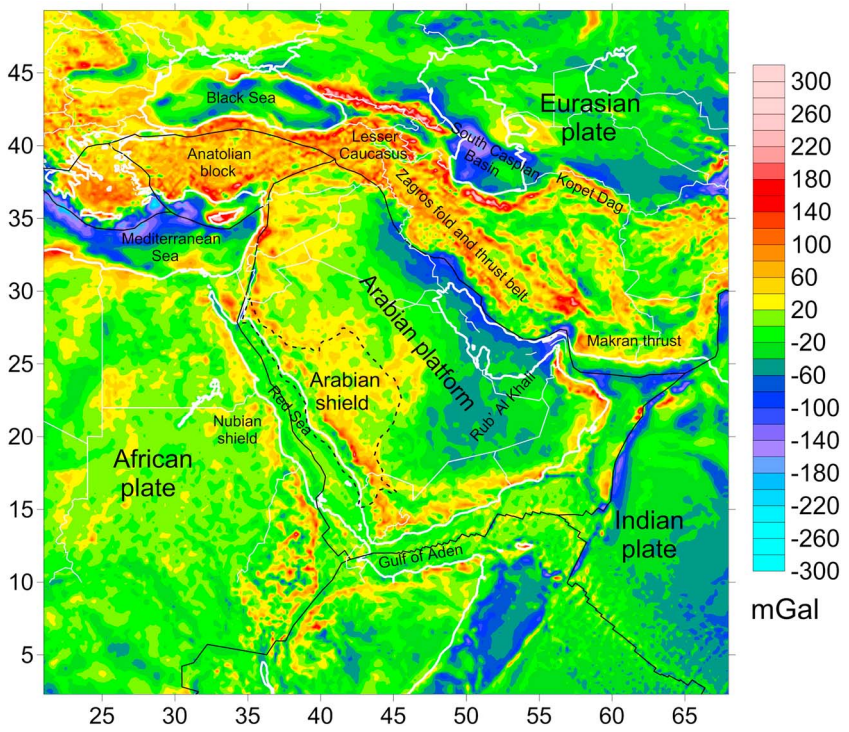

Figure 2. Initial gravity field (free air gravity disturbances), according to the EIGEN-6c4 model [*Förste et al.*, 2014], 10^{-5} m/s (mGal).

observations (for spherical harmonics exceeding ~240). In the offshore regions satellite altimetry data are used for the high-frequency part of the field. Therefore, the satellite data provide horizontal resolution up to about 83 km, which is more than sufficient for this regional study (the maximal resolution of the crustal model is $1° \times 1°$). It has been clearly demonstrated that the new satellite-based gravity models provide a revolutionary tool to study continental areas not sufficiently covered by terrestrial observations [e.g., *Braitenberg*, 2015]. The initial gravity field (Figure 2) is represented by free air gravity disturbances at the Earth surface, which are more suitable than gravity anomalies for geophysical purposes [e.g., *Hackney and Featherstone*, 2003].

2.2. Model of the Crust

A 3-D crustal model for Asia and the surrounding regions [*Stolk et al.*, 2013], which also includes the Middle East, is employed to calculate the gravity effect of the crust. The structure of the crust is based on the most complete data set, compiled by the U.S. Geological Survey (*Mooney* [2007] with updates up to 2013), and uses a revised methodology to interpolate these data, which also gives uncertainties in the interpolation. The model provides properties of the sedimentary layer and three layers of the crystalline crust. Besides thickness, the model describes variations of seismic velocity and density within each layer [*Stolk et al.*, 2013]. Within the crystalline crust the density variations are obtained from velocities using the experimental relationships of *Christensen and Mooney* [1995]. In the study area the vertically averaged density of the crystalline crust varies from 2731 kg/m^3 to 3043 kg/m^3 (average = 2911 and RMS = 42 kg/m^3), which corresponds to V_p variations in the range of 6.05–6.98 km/s (average = 6.57 and RMS = 0.12 km/s). The vertical density distribution in the sedimentary layer is characterized by a specific density-depth relationship for each basin constrained by seismic and geological data [*Stolk et al.*, 2013]. Furthermore, the model has been improved for the study area using recent compilations of the Moho and sediments [*Kaban et al.*, 2015b]. The main improvements are made for the model of sedimentary basins (Figure 3a). The Moho map, which represents the intralithospheric boundary with the largest density contrast, is shown in Figure 3b. For marginal areas the global model of the crust (CRUST1.0) [*Laske et al.*, 2013] is employed.

2.3. Initial Model of the Upper Mantle

Initially, density variations in the upper mantle were determined from seismic velocities provided by a recent global *S* wave model SL2013sv [*Schaeffer and Lebedev*, 2013]. For gravity modeling of the upper mantle, we

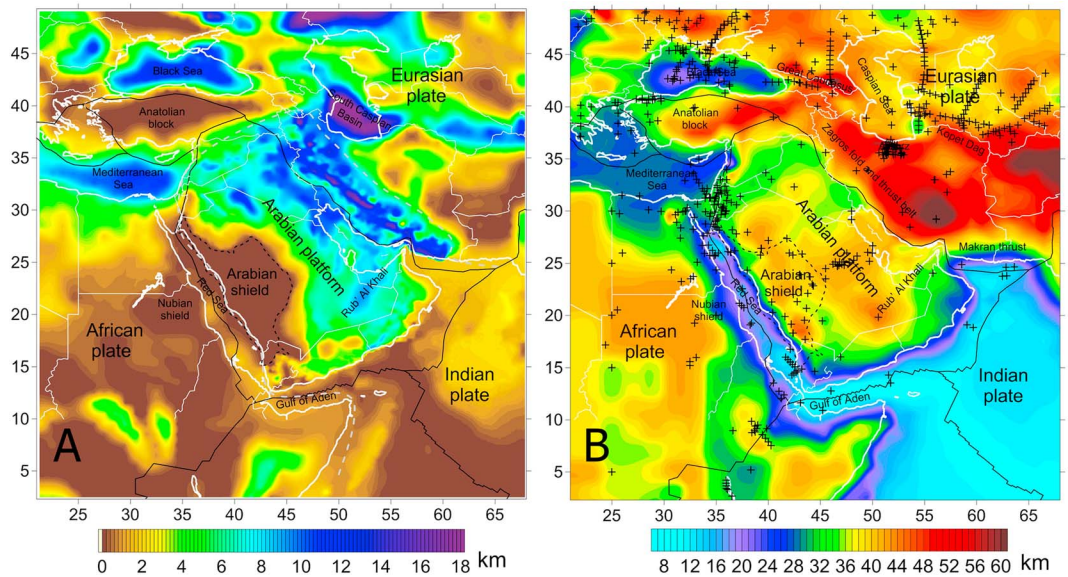

Figure 3. Model of the crust for the Middle East and surrounding area. (a) Thickness of the sedimentary layer. (b) Moho depth with respect to sea level. Initial data providing Moho depth are indicated by crosses (*Mooney* [2007] with updates up to 2015). See text for further explanation and data sources.

need information for distant zones, therefore for the territory far exceeding the study area. The employed methods also require global distribution of all parameters (see below). Although the model of *Schaeffer and Lebedev* [2013] is global, it is characterized by high horizontal resolution compared to other global models and reasonably agrees with existing regional models [e.g., *Chang and Van der Lee*, 2011].

V_s variations have been converted to temperatures and corresponding density variations as in *Kaban et al.* [2014] using the mineral physics approach of *Stixrude and Lithgow-Bertelloni* [2005]. Following this approach, which uses the Eularian finite strain formulation, we could estimate both the synthetic anharmonic velocity and density, as a function of temperature and pressure (corresponding to depths between 50 km and 300 km), of a peridotite containing four main mineral phases (olivine, OPX, CPX, and garnet). The physical parameters of the mantle are the same as in *Stixrude and Lithgow-Bertelloni* [2005], except for the elastic modulus and pressure derivatives of the mineral phases, which are taken from *Cammarano et al.* [2003]. We estimate the mantle temperatures comparing the seismic velocities of *Schaeffer and Lebedev* [2013], with the synthetic anharmonic velocities, corrected for the anelasticity effect using the attenuation model Q4 of *Cammarano et al.* [2003]. In the conversion, we assume a uniform composition (called "fertile" in *Kaban et al.* [2014]), which has not been affected by depletion of heavy constituents or other compositional changes. This composition is defined as an average of the mineral fractions constituting the "Primitive mantle" rock [*McDonough and Sun*, 1995] and the "Tecton garnet peridotite" rock [*Griffin et al.*, 2003]: Ol: 58.5%, OPX: 15%, CPX:11.5%, and Gt:15%, with a Mg# ($100 \times \mathrm{Mg}/(\mathrm{Mg}+\mathrm{Fe})$) = 89. Therefore, we assume at this stage that *S* wave velocity variations depend on temperature only. However, compositional variations can cause positive and negative density anomalies in the upper mantle, independently on the thermal regime of the area, as extensively discussed in previous studies [*Lee*, 2003; *Kaban et al.*, 2014; *Tesauro et al.*, 2014]. The calculated density and temperature variations at a depth of 80 km are shown in Figure 4.

Since composition is assumed to be uniform, the velocity, thermal, and density models are correlated. The lowest temperatures (500°–800°C) corresponding to the largest positive density variations ($>20\,\mathrm{kg/m^3}$) are found beneath the central and eastern part of the Arabian platform and along the northern part of the Eurasian plate. In the other continental areas the temperature is near or at the melting point (1300°C), and the amplitude of negative density anomalies is even larger ($< -20\,\mathrm{kg/m^3}$). These results reflect the presence of a very thin lithosphere due to upwelling of the mantle (e.g., beneath the East African rift and Arabian Shield). However, some parts of the continental collision zone (northeast from the Zagros fold belt, Lesser Caucasus, and Anatolian block) are also characterized by high temperature and a low density subcrustal layer.

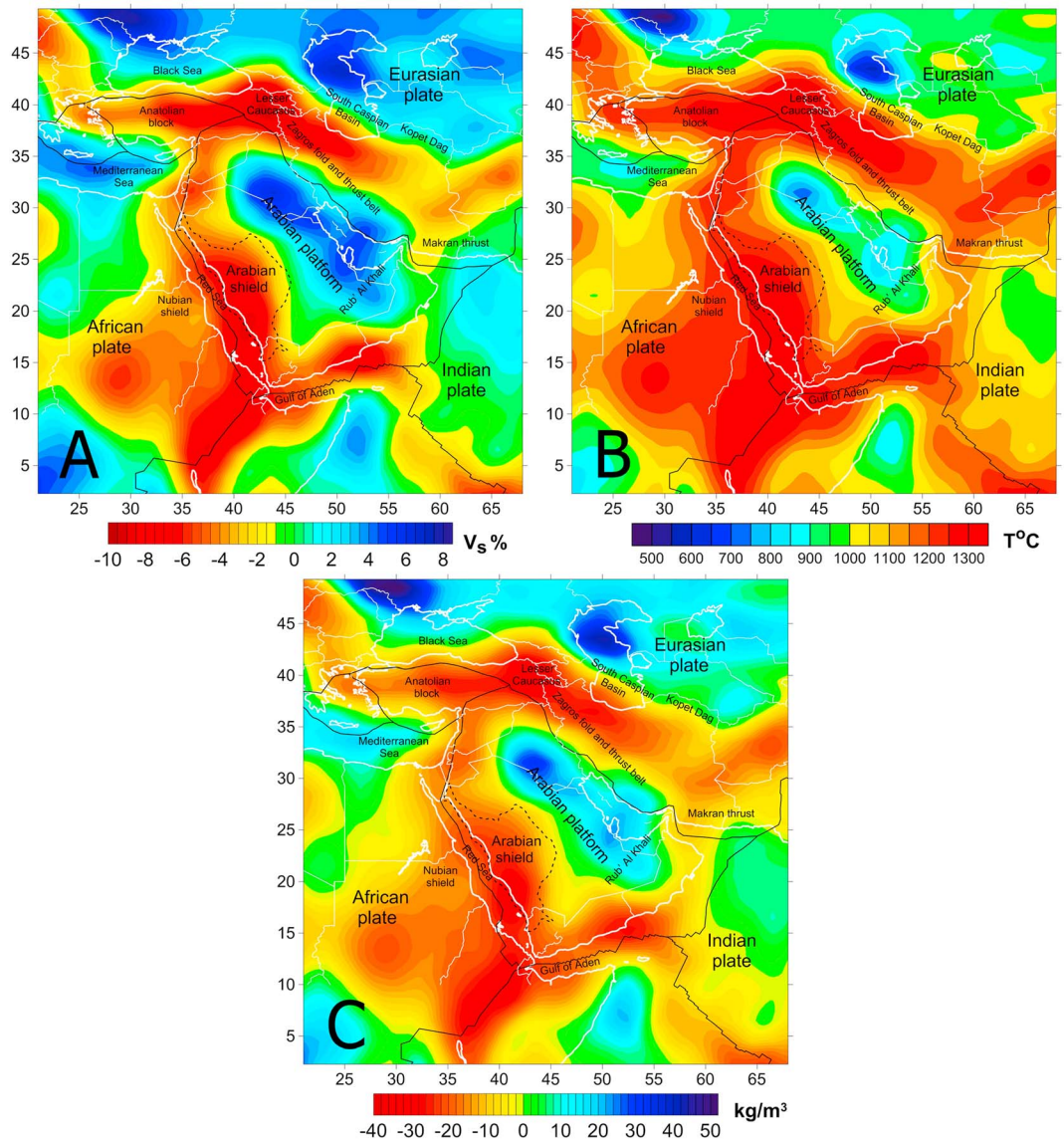

Figure 4. Initial model of the upper mantle (depth 80 km). (a) *S* wave tomography model SL2013sv [*Schaeffer and Lebedev*, 2013]. (b) Temperature variations. (c) Corresponding density variations relative to a reference density of 3370 kg/m^3.

In the offshore areas, the hot and low density upper mantle is observed beneath the Gulf of Aden and Red Sea spreading axis.

The uncertainties affecting the temperature and corresponding density variations depend on several factors [*Kaban et al*., 2014]. As pointed out in this paper, the uncertainties of the initial seismic velocities correspond to temperature and density deviations of ~150°C and 15 kg/m^3, respectively. However, this does not have a large effect on this study, since the initial density model is used only as a first approximation, which is later corrected to fit the gravity and residual topography fields. In this way, we can also eliminate errors related to the intrinsic uncertainties of the velocity-temperature-density conversion, which are associated with some factors (e.g., variations of composition) not considered in the first step [*Tesauro et al*., 2014].

3. Residual Mantle Gravity Anomalies and Residual Topography

To calculate the gravity impact of the crust on the observed gravity field, we employ the density variation in each crustal layer relative to a standard (reference) density-depth profile. Most of the parameters of the

Table 1. Parameters of the Reference Density Model

	Upper crust	Lower crust	Uppermost mantle	
Depth (km)	0–15	15–40	50	100
Density (kg/m^3)	2700	2940	3357	3384
		Upper mantle		
Depth (km)	150	200	250	300
Density (kg/m^3)	3419	3457	3510	3560

reference density distribution affect only an average value of the computed gravity field, which is not the focus in this type of study [*Kaban et al*., 2004]. Only the value of the standard density of the upper mantle affects the gravity field produced by Moho variations. However, plausible changes of the standard upper mantle density lead to insignificant changes of the computed field [*Mooney and Kaban*, 2010; *Kaban et al*., 2014]. This uncertainty is included in the total estimated uncertainty of the calculations (see below). The parameters of the reference density model are shown in Table 1.

The standard density model of the crust is the same as employed in previous studies by *Kaban et al*. [2004, 2014] and of *Mooney and Kaban* [2010]. Such a choice gives the possibility of directly comparing the results obtained for different regions. The reference densities in the upper mantle correspond to the global average, estimated as a function of the upper mantle temperatures obtained from the conversion of the seismic tomography model of *Schaeffer and Lebedev* [2013] assuming the fertile mantle composition [*Tesauro et al*., 2014].

The gravity effect of the crustal layers, topography, and Moho is calculated for each point on the surface. This field represents the sum of all elementary cells (tesseroids) defined by the model boundaries within the Earth. The calculations are fully 3-D, and the technical details are described in *Kaban et al*. [2015b]. Distant zones may produce significant trends related to fundamental differences, e.g., between the Northern and Southern Hemispheres [*Kaban et al*., 2004]. Therefore, variations of the model parameters are considered for the whole Earth when calculating the gravity effects at each point. Outside the study area the global crustal model (CRUST1.0) [*Laske et al*., 2013] is exploited. In some areas (Eurasia, North America, and Australia) CRUST1.0 is corrected based on recent and more detailed regional crustal models [*Tesauro et al*., 2008; *Stolk et al*., 2013; *Collins et al*., 2003]. The effect of topography (including the ice shields) and sea floor variations was also estimated taking into account variations over the whole Earth. The ETOPO1 model [*Amante and Eakins*, 2008] is employed onshore and the SRTM30_plus model [*Becker et al*., 2009] offshore. The gravity field created by the sediments, crystalline crust, and Moho is displayed in Figure 5.

The gravity effect of sediments spans the range -100–$0 \cdot 10^{-5}$ m/s^2 (mGal). The largest minima in the continental regions are found in the Arabian platform (eastern part) and along the Zagros fold belt, where the sedimentary thickness is greater than 10 km, as well as in some offshore areas (e.g., the southern part of the Caspian Sea and eastern Mediterranean and Black Sea), where the thickness of the relatively low-density sediments reach ~ 20 km. The crystalline crust produces strong positive gravity anomalies ($>250 \cdot 10^{-5}$ m/s^2) in the Zagros mountains and Great Caucasus, where its thickness is greater than 45 km and in two regions of the Arabian platform. In contrast, in most of the offshore areas the crystalline crust produces negative gravity anomalies. However, the largest gravity anomalies are generated by the Moho variations. Within the continental areas they are as large as $\pm 300 \cdot 10^{-5}$ m/s^2, with the minimum values corresponding to the areas with thick crust (e.g., Zagros Mountains). In contrast, in the oceans, where the crust is very thin, the gravity effect of the Moho exceeds $300 \cdot 10^{-5}$ m/s^2.

The total crustal gravity field, including the effects of topography and sea floor variation, has been removed from the initial free air gravity disturbances. This correction is an analog of the Bouguer correction, where the effect of topography/bathymetry is combined with the total effect of the crust down to the Moho [e.g., *Mooney and Kaban*, 2010]. Therefore, the residual gravity anomalies reflect the effect of density variations below the Moho (chiefly in the mantle) and also errors in the crustal model and density conversion. The long-wavelength effect of the deep mantle can be estimated from global dynamic models (instantaneous) as was done by *Kaban et al*. [2015b] based on the recent global model of *Petrunin et al*. [2013]. In addition, we remove the effects of the transition zone boundaries, as determined by *Kaban and Trubitsyn* [2012]. The total gravity effect of the mantle density heterogeneities below 325 km is shown in Figure 6a. This field

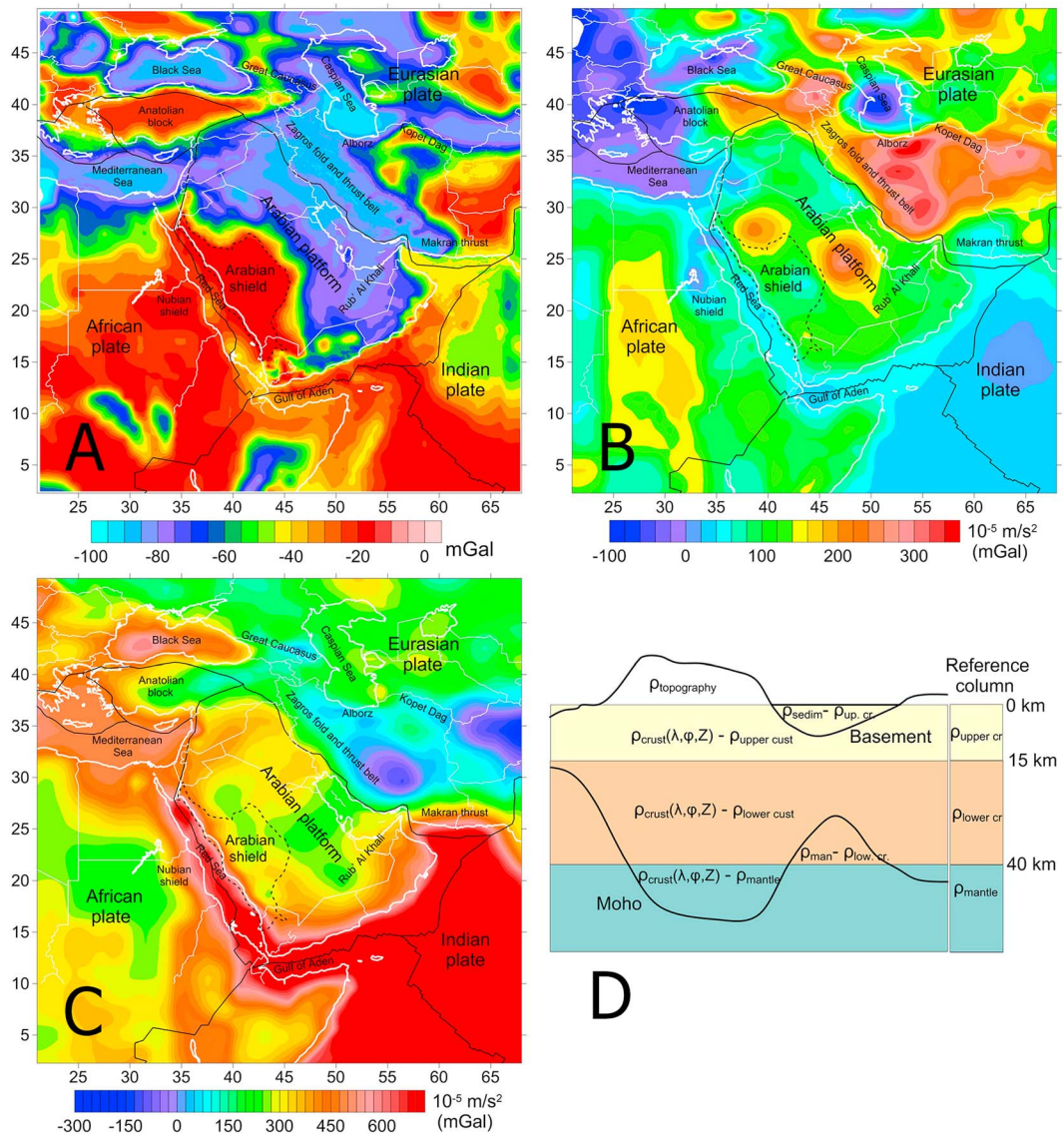

Figure 5. Gravity effect of (a) sediments, (b) crystalline crust, and (c) Moho variations estimated relative to a standard 1-D model (Table 1). (d) Cartoon explaining density anomalies used in calculations.

exhibits a smooth trend over the study area, and the amplitudes (-35 to $+15 \cdot 10^{-5}$ m/s^2) are much less than the total mantle anomaly amplitudes. The residual mantle gravity anomalies obtained after removing of the crustal and deep mantle effects are shown in Figure 7a.

The density model of the crust is also employed to estimate the residual topography (t_{res}), representing the part of the topography/bathymetry that is not balanced by the crustal structure including variations of the crust-mantle boundary [e.g., *Kaban et al.*, 2004]:

$$t_{res} = \frac{1}{\overline{\rho}}\left(\rho_{top}\right)t_{obs} + \frac{1}{\overline{\rho}}\int_0^M \Delta\rho(h)\left(\frac{R-h}{R}\right)^2 dh, \quad (1)$$

where ρ_{top} is the average density above sea level (taking into account sediments and ice); t_{obs} is the topography (zero offshore); R is the Earth radius; $\overline{\rho} = 2670$ kg/m^3 is the standard density; $\Delta\rho(h) = \rho - \rho_{ref}$ is the relative density below sea level; and h is the depth from sea level.

The residual topography is normally associated with the density structure of the mantle lithosphere and with dynamic topography supported by the mantle convection [e.g., *Steinberger and Calderwood*, 2006]. However,

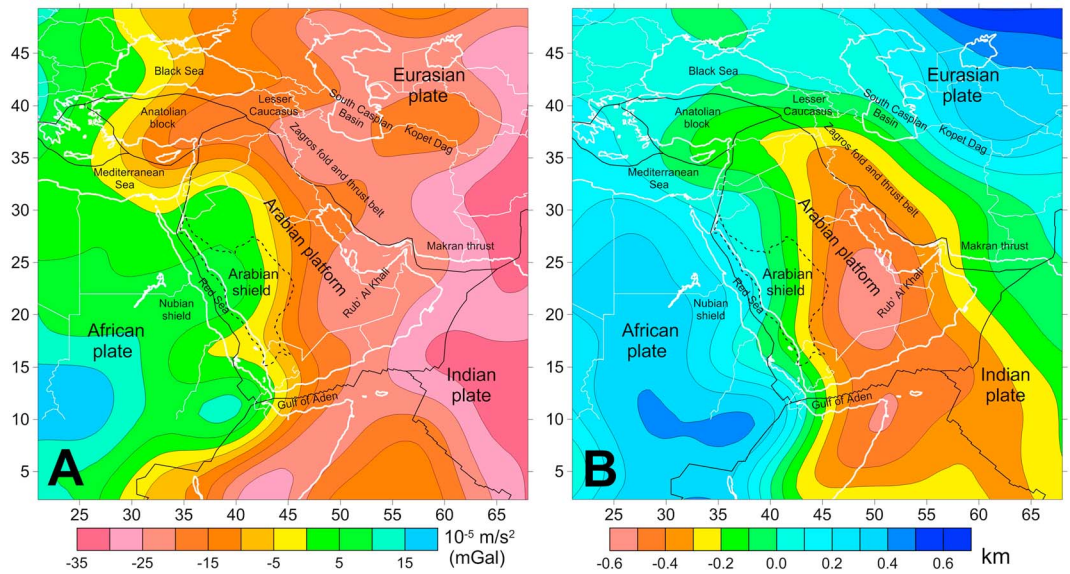

Figure 6. Effect of density variations below 325 km. (a) Gravity field and (b) Dynamic topography.

more factors controlling this parameter should be considered [*Kaban et al.*, 2004]. Relatively short-wavelength variations of t_{res} relate to the load supported by lithospheric stresses, since equation (1) implies a local isostatic condition. Therefore, we do not consider local anomalies of the residual topography while constructing the density model of the mantle. Large-scale variations of t_{res} could also be associated with noncompensated deformations remaining after deglaciation. However, these deformations are relatively small (up to ~0.2 km) and are not present in the study area. The effect of the deep mantle below 325 km (bottom of the model) is estimated in the same way as the gravity effect using the global dynamic model based on *Kaban and Trubitsyn* [2012] and *Petrunin et al.* [2013]. The amplitude of this field (Figure 6b) is relatively small (±0.5 km) and is significantly less than the total dynamic topography over the Arabian plate estimated previously by various methods [e.g., *Faccenna et al.*, 2013; *Wilson et al.*, 2014]. Therefore, the effect of the upper mantle dominates in the noncompensated residual topography (Figure 7b).

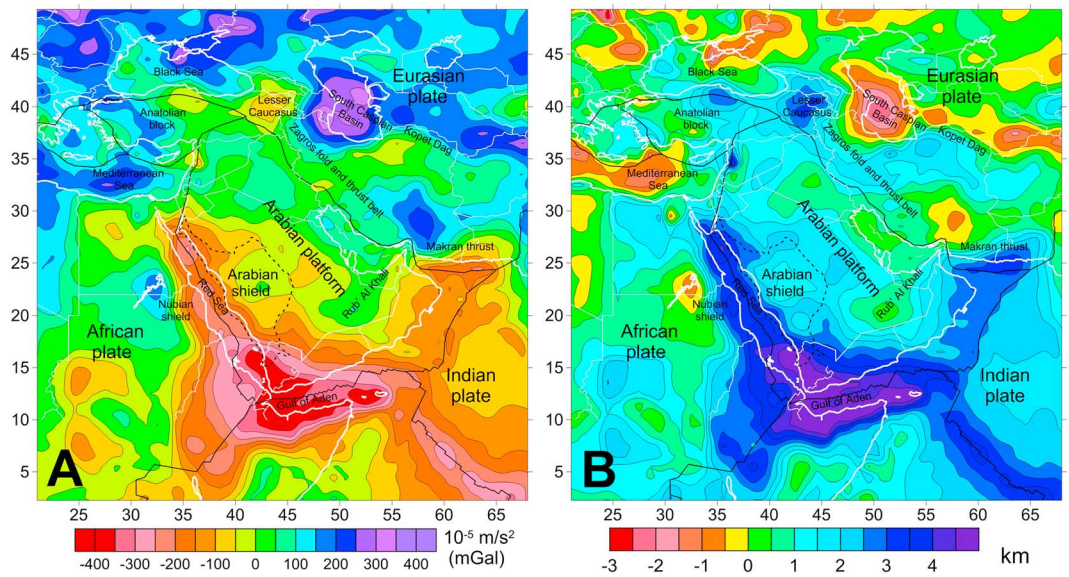

Figure 7. (a) Residual mantle gravity anomalies and (b) residual topography. Both fields are estimated by removing the effects of the crust and of the mantle density variations below 325 km (see text). The residual topography is adjusted to the density of 2670 kg/m^3.

Table 2. Potential Errors of the Residual Gravity and Residual Topography [*Mooney and Kaban*, 2010][a]

	Sediments	Crystalline Crust	Moho	Standard Density of the Upper Mantle
Gravity field 10^{-5} m/s^2 (mGal)	10–15	25–50	30–60	10
Residual topography (km)	0.09–0.14	0.22–0.44	0.27–0.54	0.09

[a]The minimum values correspond to well-studied regions and vice versa.

Mooney and Kaban [2010] analyze potential errors of the residual gravity and residual topography. They are summarized in Table 2. We consider the uncertainties to be related to relatively broad anomalies of several hundred kilometers or more. Uncertainties of the initial gravity model [*Förste et al*., 2014] are low compared to those introduced by the crustal model. For relatively large-scale anomalies, which are considered in this study, the error in the gravity field from the sedimentary model may reach $10–15 \cdot 10^{-5}$ m/s^2 (mGal) [*Stolk et al*., 2013]. *Christensen and Mooney* [1995] provide a value of ±50 kg/m^3 for the uncertainty of the crystalline crust density for an individual layer. Considering the crustal layers to be independent, the contribution of the crystalline crust may reach 25 to $50 \cdot 10^{-5}$ m/s^2 depending on the thickness [*Mooney and Kaban*, 2010]. Uncertainties related to the Moho depth [*Stolk et al*., 2013], for relatively extended anomalies, could vary from $30 \cdot 10^{-5}$ m/s^2 for areas well constrained by seismic observations to ~$60 \cdot 10^{-5}$ m/s^2 for poorly constrained areas. These estimates are summarized in Table 2.

The uncertainties in Table 2 are considered independent and random, thus the standard deviation of the residual gravity anomalies ranges from ~$40 \cdot 10^{-5}$ m/s^2 (mGal) for areas well constrained by seismic measurements, to ~$75 \cdot 10^{-5}$ m/s^2 for continental areas with irregular seismic networks [*Mooney and Kaban*, 2010]. Correspondingly, the standard deviation of the residual topography ranges from ~0.35 km to ~0.65 km. There exist several areas in the study region, where the crustal structure is not constrained by seismic experiments, such as the territories of Afghanistan, Pakistan, and some parts of Africa, except for the area adjoining the Red Sea and Afar, which is covered by seismic data. For these regions the results obtained are not realistic and will not be discussed.

The calculated variations of the residual mantle anomalies and residual topography in the study area reach $\pm 400 \cdot 10^{-5}$ m/s^2 (mGal) and from −4 to +5 km, correspondingly (Figure 7). Therefore, for most of the study area, they exceed potential determination errors. Both the residual gravity anomalies and topography show similar patterns but with opposite sign, since they depend on density variations in the upper mantle. However, remarkable differences exist because of the distinct dependence of these parameters on the depth and wavelength of the mantle density anomalies [*Kaban et al*., 2015a]. Therefore, the inversion of both parameters gives the possibility of increasing the vertical resolution of the density models, as discussed in section 4. Another difference between these parameters is that for the residual topography it is possible to consider absolute values, which are directly related to the reference density model. In contrast, the average level of the residual gravity anomalies strongly depends on the density structure of remote areas [*Kaban et al*., 2004]. Therefore, we consider only relative variations of the gravity anomalies.

Negative gravity anomalies (and correspondingly, positive residual topography) characterize the Gulf of Aden, Red Sea, and the mid-oceanic ridge with the absolute minimum (maximum) over the Afar triple junction ($-400 \cdot 10^{-5}$ m/s^2 and +5 km, correspondingly, Figure 7), which are likely related to the hot mantle (Figure 4). Since the main patterns of these parameters are mirrored, we limit the further discussion to the gravity anomalies. The mid-oceanic ridge is also characterized by negative residual mantle anomalies, as we would expect from its hot thermal conditions. In the continental area, negative residual anomalies are found in the northern part of the Anatolian block along the North Anatolian fault, Lesser Caucasus, and over the Zagros fold and thrust belt (~ $-200 \cdot 10^{-5}$ m/s^2). The maximum gravity anomaly (up to $400 \cdot 10^{-5}$ m/s^2, Figure 7) characterizes the South Caspian basin and significant positive anomalies are also found in the South Mediterranean and the adjoining part of the East European Platform. In contrast to previous results [e.g., *Kaban et al*., 2015b] and seismic tomography studies [e.g., *Schaeffer and Lebedev*, 2013], we do not find a large difference in the residual mantle gravity and residual topography between the Arabian platform and Arabian Shield except for the area adjoining the Red Sea (Figure 7). In further analysis we will try to determine if this result is relevant to all mantle layers or if both fields represent a combination of different (and possibly opposite) effects at various depths.

4. Three-Dimensional Density Model of the Mantle

The mantle gravity anomalies and residual topography are inverted to constrain the density structure of the upper mantle. The use of both parameters provides the possibility of resolving the 3-D density distribution more reliably than by interpreting only the gravity field, since they depend differently on the depth and size of the original density anomaly [*Kaban et al*., 2015a]. This is an Occam-type inversion, which is constrained by the initial density model based on seismic tomography (ρ_{ini}, Figure 4):

$$\min\{||A\rho - g_{\text{res}}||^2 + k||B\rho - t_{\text{res}}||^2 + \alpha||\rho - \rho_{\text{ini}}||^2\}, \quad (2)$$

where A is the integral operator that converts density variations ρ into gravity anomalies, B—to topography undulations, t_{res} is the residual topography, g_{res}—residual gravity anomaly, $k = 2\pi G\rho_t$ is the coefficient normalizing topography variation relative to the gravity (G is the gravitational constant), and α is the damping factor.

The model setup is the same as in *Kaban et al*. [2015b]. The gravity anomalies, residual topography, and initial model of the mantle have been decomposed into spherical harmonic coefficients and a solution was found separately for each coefficient. Outside the study area, we employ the same initial density model based on the global seismic tomography of *Schaeffer and Lebedev* [2013]. Density variations are determined for seven layers with central depths at 15, 50, 100, 150, 200, 250, and 300 km. The upper layer is introduced to correct potential errors of the crustal model in the continental area. To compute of the topography undulations we use the viscosity distribution based on global dynamic models constrained by mineral physics [*Steinberger and Calderwood*, 2006]. The value of the damping factor is assigned based on the amplitude of the inverted densities and of the residuals (not adjusted parts of both fields) as described in details in *Kaban et al*. [2015b, supporting information]. Additional details and numerical tests, which prove stability of the obtained results to plausible variations of the mantle viscosity and damping factor, are provided in *Kaban et al*. [2015a, supporting information]. The results of the inversion are shown in Figures 8 and 9.

The additional density variations, which supplement the initial model reach ±60 kg/m^3 (Figures 8c, 8d, and 9). We identify three main factors, which may be associated with the corrections of the initial density model. First, they improve the resolution of the initial model based on the seismic tomography. Second, the corrections account for factors that were not considered while converting seismic velocities into density variations, such as those related to changes in composition [*Tesauro et al*., 2014]. The presence of water (or other volatiles) can also significantly bias the conversion of velocities into density variations [e.g., *Goes et al*., 2000]. Furthermore, the density correction for the uppermost mantle may be related to errors of the initial model of the crust. For example, if the Moho depth is underestimated, the correction will be negative to compensate the effect of the uplifted mantle material and vice versa. A similar effect could be associated with incorrect density of the lower crust. It should be also taken into account that the horizontal resolution of the inversion decreases with depth because of damping [*Kaban et al*., 2015a]. These factors are considered in the interpretation of the obtained results.

5. Discussion

The resolution of the final density model is improved compared to the initial one, which results in a better fit to the tectonic division of the study area. For instance, the broad negative anomaly, spreading from East Africa via the Nubian Shield and the Red Sea to the Arabian Shield, is localized in the final model in the uppermost mantle under the Red Sea (Figure 9 and section 2). Below 100 km this anomaly extends under the Arabian Shield, which agrees with the recent regional seismic tomography models [*Chang et al*., 2011; *El Khrepy et al*., 2015]. The negative mantle density anomalies associated with the hot mantle under the Gulf of Aden and Afar remain basically the same, but the amplitude in the Gulf of Aden is significantly increased likely due to insufficient resolution of the initial tomography model (Figure 9 and section 5). The minimum is shifted from the Red Sea to the Gulf, where it is likely associated with the most active mantle upwelling [*Bosworth et al*., 2005] (Figure 9 and section 4). This negative anomaly extends under Yemen, which is also affected by upwelling of mantle material, in agreement with recent tomography studies [*Korostelev et al*., 2014; *Corbeau et al*., 2014]. Furthermore, the Red Sea is clearly divided into two distinct parts. The negative density anomaly in the northern part extends to the depth ~150 km (Figure 9 and sections 1 and 4). In contrast, the same anomaly in the southern part extends to the bottom of the model and is likely linked with upwelling originating in the deep mantle (Figure 9 and sections 3 and 4). The amplitude of the negative

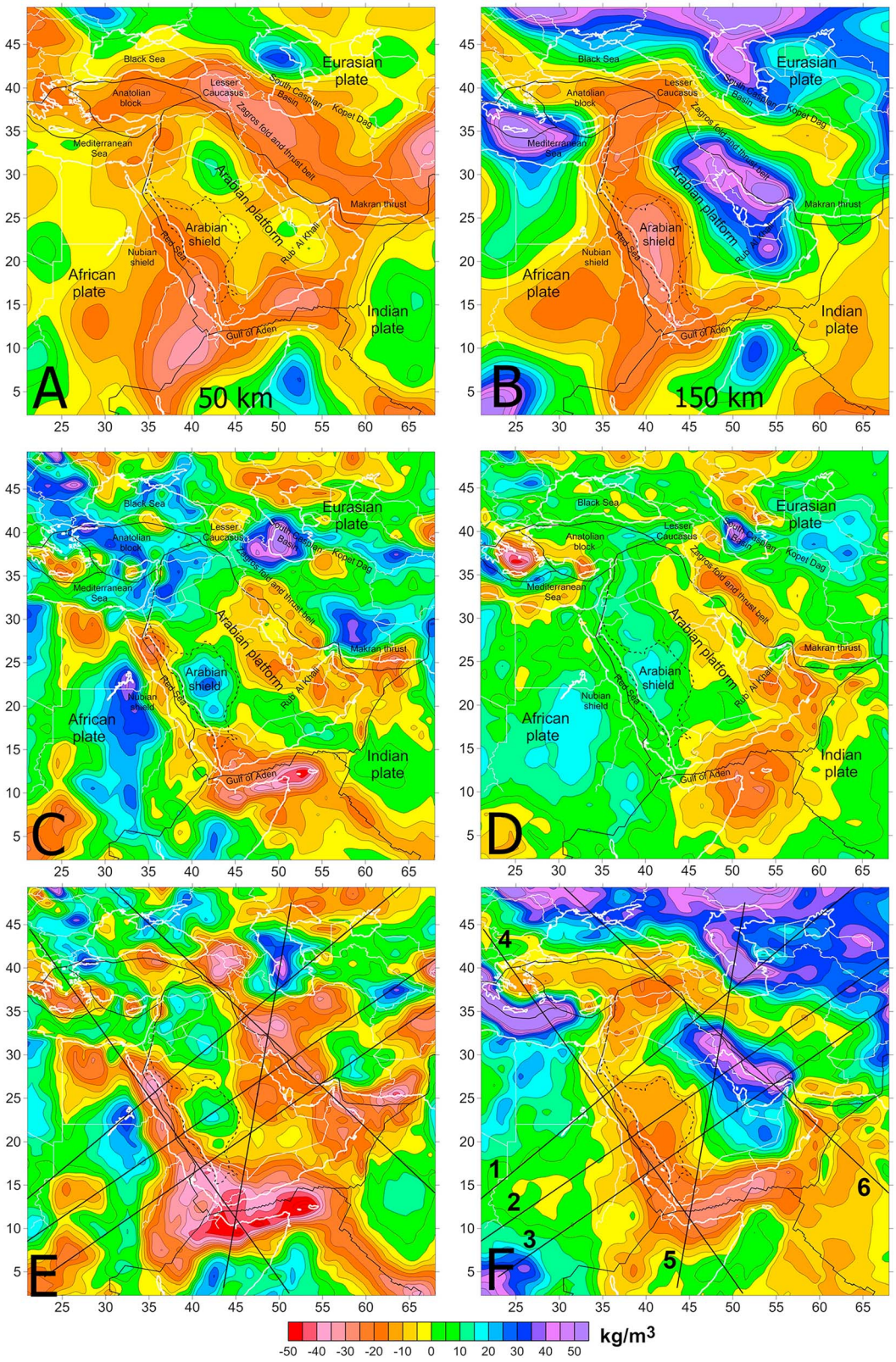

Figure 8. Density model of the upper mantle. (a, c, and e) Density anomalies at 50 km depth (reference density is 3357 kg/m^3) and (b, d, and f) at 150 km (reference density is 3419 kg/m^3). (a, b) Initial density model, Figure 4. (c, d) Correction obtained in the inversion of the residual mantle anomalies and residual topography (Figure 7). (e, f) Final density variations after adjustment. Black lines show position of sections in Figure 9.

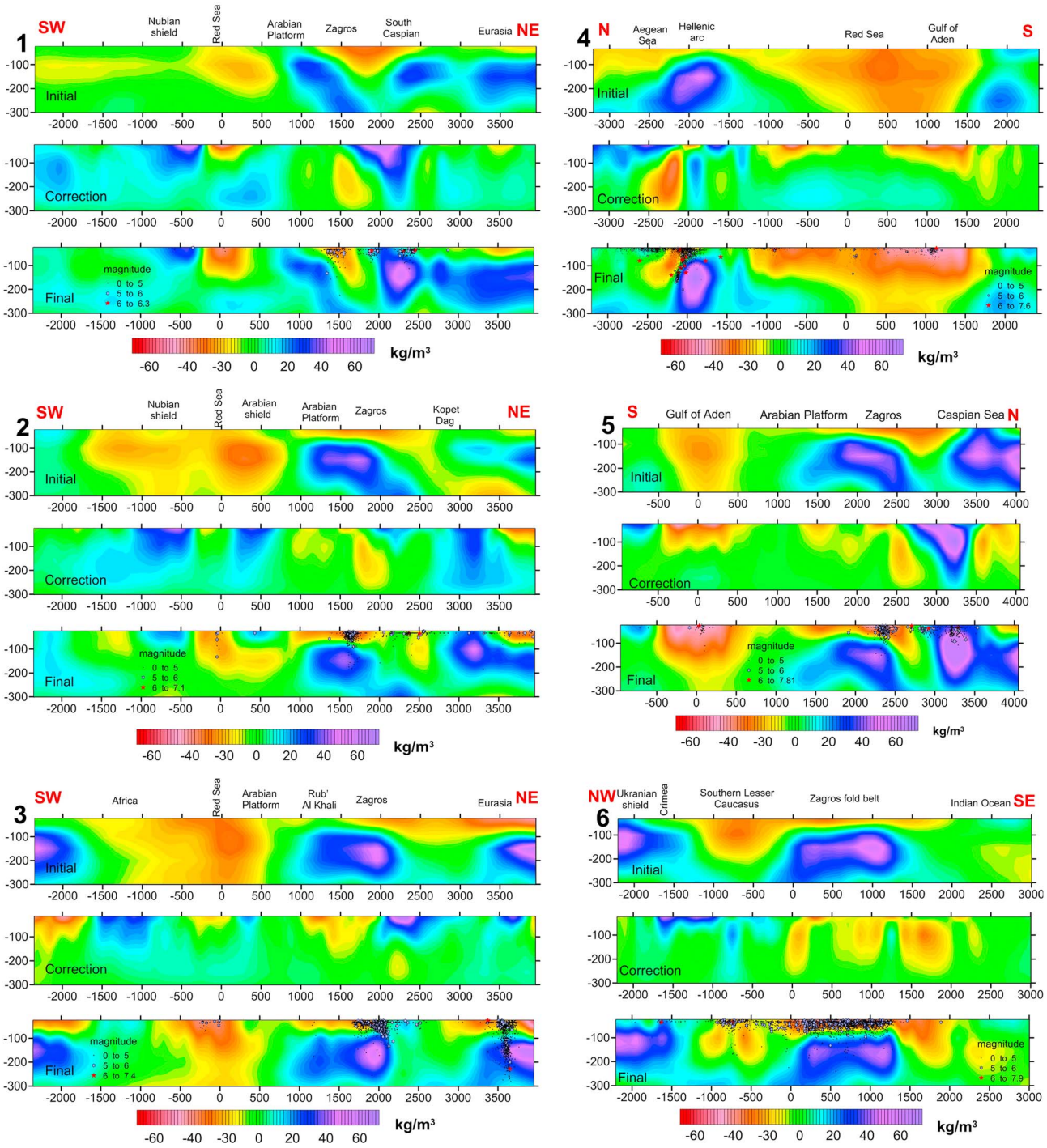

Figure 9. Density variations in the upper mantle along six sections (Figure 8). The initial model is based on the tomography model of *Schaeffer and Lebedev* [2013]. The correction is obtained from inversion of the residual mantle anomalies and residual topography (Figure 7). The adjusted density distribution is shown in the bottom sections. Earthquake hypocenters are from the ISC-GEM catalog [*Storchak et al.*, 2013].

density anomaly is decreased in the center of the Red Sea, which is associated with increased earthquake depth of (Figure 9 and section 4). Furthermore, the uppermost part of the anomaly in the central Red Sea (up to a depth of ~100 km) is shifted toward Africa (Figure 9 and section 2). Previously, whether the Red Sea represents an active or a passive rifting zone has been strongly debated [*Hansen et al.*, 2007]. Based on our results, we suggest that the northern Red Sea may be characterized by a passive regime, where the

gap between the diverging plates is filled by hot asthenospheric material. In contrast, the southern Red Sea could be associated with active rifting initiated by mantle upwelling.

In agreement with recent studies [e.g., *El Khrepy et al*., 2015; *Kaban et al*., 2015b], we find a fundamental difference in the lithosphere structure between the Arabian Platform and the Arabian Shield. A new finding is the reversal of mantle properties at depths of 75–100 km (Figures 8 and 9 and section 2). The uppermost mantle (to a depth of 70–80 km) under the Arabian Shield is characterized by high densities (Figure 9 and section 2). Since the crustal model in this area is robust [*Kaban et al*., 2015b], we cannot attribute this feature to uncertainties of the crustal structure. Instead, we suggest that the upper mantle has been rejuvenated by a phase of mantle upwelling at ca. 800 Ma [*Stern and Johnson*, 2010]. *O'Reilly and Griffin* [2012] pointed out that metasomatic refertilization of the cratonic upper mantle increases its density and decreases seismic velocities. For this reason, the high-density uppermost layer of the mantle is less visible in seismic tomography than in the combined seismic-gravity model. It should be noted that the same feature is observed in the Nubian Shield (Figures 8 and 9 and sections 1 and 2), which is symmetrically located west of the Red Sea. However, the results for the Nubian Shield are preliminary because the crustal model is less reliable. The relatively dense subcrustal layer of the Arabian Shield is underlain by a low dense mantle below a depth of ~100 km, and the anomaly is connected to the minimum under the Red Sea (Figure 9 and sections 1–3).

The Arabian Platform is characterized by high-density mantle at the depths 100–230 km, in agreement with previous studies [*Schaeffer and Lebedev*, 2013; *El Khrepy et al*., 2015]. In contrast, the uppermost mantle has relatively low densities in the central part of the platform and normal densities elsewhere (Figures 8 and 9). Therefore, two reversed dipole structures, located under the Arabian Shield and Platform, produce not so different gravity effects and are not clearly visible in the residual gravity anomalies (Figure 7) but appear in the inversion constrained by the tomography model. Unlike the mantle under the Arabian Shield, the mantle under the Platform has not been reworked by upwelling. Therefore, this low-density anomaly may be associated with depleted material, as indicated by geochemical data [*Priestley et al*., 2012]. Furthermore, the localized high-density anomaly beneath the Arabian Platform dips sharply toward the Zagros thrust and fold belt (Figure 9 and sections 1–3). These sharp changes outline the subducting continental plate with possible delamination below a depth of 200 km (Figure 9 and sections 2). The density of the uppermost mantle layer (down to approximately 100–140 km) decreases toward the Zagros Mountains, in agreement with seismic studies [e.g., *Priestley et al*., 2012]. These authors argue that the negative velocity anomaly may be associated with lithospheric melts and depleted material. Further to the northwest, the low-density zone extends toward the Lesser Caucasus.

One of the largest positive density anomalies in the upper mantle ($>$60 kg/m^3) is found under the Caspian Sea. Compared to the initial model, this anomaly is shifted to the south and is localized under the South Caspian basin (Figures 8 and 9 and section 1). The strong South Caspian block is bounded by active seismic zones. To the north, another positive anomaly is coincident with the Pre-Caspian basin. The South Caspian basin is characterized by very thick sediments (~20 km, Figure 3) and a very thin crystalline crust with low velocities corresponding to those of the upper crust [*Stolk et al*., 2013]. Several basins (in particularly, oil-rich ones) are characterized by similar structure [*Cloetingh and Burov*, 2011]. *Mooney and Kaban* [2010] identified a high-density block in the subcrustal layer under the Gulf of Mexico. They suggest that this anomaly is related to an eclogite layer, which is responsible for fast subsidence of this basin. A similar feature has been found under the Barents Sea [*Ebbing et al*., 2007; *Braitenberg and Ebbing*, 2009; *Gac et al*., 2013] and under the West Siberian basin [*Braitenberg and Ebbing*, 2009]. Therefore, the mechanism associated with the gabbro-eclogite conversion can be important for the evolution of sedimentary basins and may have influenced the thermal maturation of sediments [*Gac et al*., 2014].

A strong inclined positive anomaly in the upper mantle is found under the Hellenic arc, which outlines the subduction of the African plate (Figure 9 and section 4). The gravity correction principally changes the initial structure in this area (Figure 9 and section 4). A strong negative density anomaly is revealed that corresponds to the back-arc volcanic zone, which is consistent with local studies [e.g., *Polatidis et al*., 2003; *Papazachos et al*., 2000]. The boundary between the subducting slab and the low-density back-arc block plainly corresponds to the Benioff-Wadati seismic zone, as we can see from the earthquakes distribution (Figure 9 and section 4).

The part of Eurasia that borders the study area is mainly characterized by positive density anomalies in the upper mantle with amplitude of up to 50 kg/m^3 (Figure 9 and section 6). In the northwestern corner, the anomaly corresponds to the Ukrainian Shield, the old (3.2–3.8 Ga) and cold part of the East European craton [e.g., *Yegorova et al*., 2004]. In the northeast, the obtained model shows a sharp density contrast in the mantle

between the Kopet Dag and Turan plate with a relatively high-density mantle (>40 kg/m^3). The density contrast is significantly sharpened in the inversion, showing partial underthrust of the Turan plate under the Kopet Dag ridge (Figure 9 and section 2). This feature has already been proposed based on the results of flexural modeling of the lithosphere [*Artemjev and Kaban*, 1994]. The boundary between the Kopet Dag and Turan plate is clearly marked by the seismicity distribution (Figure 9 and section 2).

6. Conclusions

A three-dimensional density model of the lithosphere and upper mantle is developed for the Middle East and surrounding area based on integration of seismic, gravity, and seismic tomography data. The main results are as follows.

1. Residual mantle gravity anomalies and residual topography are calculated by removing the effects of the crust and deep mantle from the observed fields. The amplitude of these anomalies reaches $\pm 400 \cdot 10^{-5}$ m/s^2 (mGal) and $-4 \div +5$ km, respectively, and significantly exceeds their uncertainties. The estimated anomalies show a strong heterogeneity of the upper mantle directly related to the tectonic history of the Middle East and to the ongoing tectonic processes in agreement with the seismicity pattern, which delineates different types of tectonic process in the study region.
2. By jointly inverting the residual gravity anomalies and residual topography we adjusted the initial density model, which is based on seismic tomography, and constructed a 3-D density model of the mantle. The obtained density variations reach ±60 kg/m^3. The resolution of the final model is remarkably improved compared to the initial one and corresponds well to the tectonic division of the region.
3. Strong density variations within the lithosphere are found in the Arabian plate. The Arabian Shield and Arabian Platform represent two reversed dipole structures. The subcrustal layer in the Arabian Shield is relatively dense down to a depth of ~80 km. This anomaly may be explained by metasomatic refertilization of the mantle rocks because of mantle upwelling at circa 800 Ma [*Stern and Johnson*, 2010; *O'Reilly and Griffin*, 2012]. In contrast, the lower part of the upper mantle is characterized by low density likely associated with the hot upwelling mantle, which is connected to the low-density conduit under the Red Sea. This feature explains why the Arabian Shield is weak relative to the Platform, as was determined from estimates of the effective elastic thickness [*Chen et al*., 2015]. The density structure of the Arabian Platform is vertically reversed. The uppermost layer in the central part of the shield is characterized by relatively low densities, probably due to depletion of high-density constituents [e.g., *Priestley et al*., 2012]. On the other hand, the lower part of the upper mantle is relatively dense up to a depth of ~200 km (bottom of the lithosphere).
4. In agreement with previous studies, the rift zones and mid-oceanic ridges in the study area are characterized by a low-density mantle. It appears that the density structures of the northern and southern parts of the Red Sea are different. The low-density mantle under the northern Red Sea is limited to a depth of ~150 km, while in the southern part, it extends to the bottom of the model and is likely linked to a mantle plume. On the other hand, low densities in the uppermost mantle (predominantly up to a depth of ~120 km) are observed in the Zagros belt, the Lesser Caucasus, and the North Anatolian block (Figure 9).
5. We observe the high-density lithosphere of the Arabian plate subducting under Eurasia along the Zagros belt and of the African plate subducting under the Aegean block. In the northeastern part of the study area we identify the dense lithosphere of the Turan plate, which underthrusts the Kopet Dag.
6. A very dense mantle is found under the South Caspian basin. The density structure of this basin is very similar to the structure of the Gulf of Mexico [*Kaban et al*., 2014] and of the Eastern Barents Sea [*Braitenberg and Ebbing*, 2009, *Gac et al*., 2013]. We suggest that the increase in density is associated with an eclogite layer, which is responsible for the fast subsidence of these basins. A dense upper mantle is also revealed under the Pre-Caspian basin and the Ukrainian Shield in the northern margin of the study area.

Acknowledgments
We thank anonymous reviewers for their extensive comments that have greatly improved the manuscript. The authors extend their appreciation to the Deanship of Scientific Research at King Saud University (Saudi Arabia) for funding the work through the research group project (RG-1435-027). This study was also supported by GeoForschungsZentrum, Potsdam, Utrecht University, and the Netherlands Centre ISES. We are thankful to Sierd Cloetingh for his suggestions on an earlier version of this paper. The data for this paper are available by contacting the corresponding author at kaban@gfz-potsdam.de.

References

Agrawal, M., J. Pulliam, M. K. Sen, U. Dutta, M. E. Pasyanos, and R. Mellors (2015), Crustal and uppermost mantle structure in the Middle East: Assessing constraints provided by jointly modelling Ps and Sp receiver functions and Rayleigh wave group velocity dispersion curves, *Geophys. J. Int*., *201*(2), 783–810.

Amante, C., and B. W. Eakins (2008), ETOPO1 1 Arc-Minute Global Relief Model: Procedures, data sources and analysis, Natl. Geophys. Data Cent., NESDIS, NOAA, U.S. Dep. of Commerce, Boulder, Colo., Aug.

Artemjev, M. E., and M. K. Kaban (1994), Density inhomogeneities, isostasy and flexural rigidity of the lithosphere in the Transcaspian region, *Tectonophysics*, *240*, 281–297.

Becker, J. J., et al. (2009), Global bathymetry and elevation data at 30 arc seconds resolution: SRTM30_PLUS, *Mar. Geod.*, *32*(4), 355–371.
Bosworth, W., P. Huchon, and K. McClay (2005), The red sea and gulf of Aden basins, *J. Afr. Earth Sci.*, *43*(1), 334–378.
Braitenberg, C. (2015), Exploration of tectonic structures with GOCE in Africa and across-continents, *Int. J. Appl. Earth Obs. Geoinf.*, *35*, 88–95.
Braitenberg, C., and J. Ebbing (2009), The GRACE-satellite gravity field in analysing large scale, cratonic or intracratonic basins, *Geophys. Prospect.*, *57*, 559–571, doi:10.1111/j.1365-2478.2009.00793.x.
Cammarano, F., S. Goes, P. Vacher, and D. Giardini (2003), Inferring upper-mantle temperatures from seismic velocities, *Phys. Earth Planet. Inter.*, *138*, 197–222, doi:10.1016/S00319201(03)00156-0.
Chang, S. J., and S. Van der Lee (2011), Mantle plumes and associated flow beneath Arabia and East Africa, *Earth Planet. Sci. Lett.*, *302*(3), 448–454.
Chang, S. J., M. Merino, S. Van der Lee, S. Stein, and C. A. Stein (2011), Mantle flow beneath Arabia offset from the opening Red Sea, *Geophys. Res. Lett.*, *38*, L04301, doi:10.1029/2010GL045852.
Chen, B., M. K. Kaban, S. El Khrepy, and N. Al-Arifi (2015), Effective elastic thickness of the Arabian plate: Weak shield versus strong platform, *Geophys. Res. Lett.*, *42*, 3298–3304, doi:10.1002/2015GL063725.
Christensen, N. I., and W. D. Mooney (1995), Seismic velocity structure and composition of the continental crust: A global review, *J. Geophys. Res.*, *100*, 9761–9788, doi:10.1029/95JB00259.
Cloetingh, S., and E. Burov (2011), Lithospheric folding and sedimentary basin evolution: A review and analysis of formation mechanisms, *Basin Res.*, *23*, 257–290, doi:10.1111/j.1365-2117.2010.00490.x.
Collins, C. D. N., B. J. Drummond, and M. G. Nicoll (2003), Crustal thickness patterns in the Australian continent, *Geol. Soc. Australia Spec. Publ., 22*, and *Geol. Soc. Am. Spec. Pap., 372*, 121–128.
Corbeau, J., et al. (2014), Uppermost mantle velocity from *Pn* tomography in the Gulf of Aden, *Geosphere*, *10*, 958–968, doi:10.1130/ges01052.1.
Dewey, J. F., and A. C. Şengör (1979), Aegean and surrounding regions: Complex multiplate and continuum tectonics in a convergent zone, *Geol. Soc. Am. Bull.*, *90*(1), 84–92.
Ebbing, J., C. Braitenberg, and S. Wienecke (2007), Insights into the lithospheric structure and the tectonic setting of the Barents Sea region from isostatic considerations, *Geophys. J. Int.*, *171*, 1390–1403, doi:10.1111/j.1365-246X.2007.03602.x.
El Khrepy, S., I. Koulakov, E. Burov, S. Cloetingh, N. Al-arifi, and N. Bushenkova (2015), Seismic tomography imaging beneath the Arabian Peninsula and Red Sea, in *EGU General Assembly (2015, April) Conference Abstracts*, vol. 17, pp. 1321.
Faccenna, C., T. W. Becker, L. Jolivet, and M. Keskin (2013), Mantle convection in the Middle East: Reconciling Afar upwelling, Arabia indentation and Aegean trench rollback, *Earth Planet. Sci. Lett.*, *375*, 254–269.
Förste, C., et al. (2014), EIGEN-6C4—The latest combined global gravity field model including GOCE data up to degree and order 1949 of GFZ Potsdam and GRGS Toulouse, in *EGU General Assembly Conference Abstracts (2014, May)*, vol. 16, pp. 3707.
Gac, S., R. S. Huismans, N. S. C. Simon, Y. Y. Podladchikov, and J. I. Faleide (2013), Formation of intracratonic basins by lithospheric shortening and phase changes: A case study from the ultra-deep East Barents Sea basin, *Terra Nova*, *25*, 459–464, doi:10.1111/ter.12057.
Gac, S., R. S. Huisman, N. S. C. Simon, J.-I. Faleide, and Y. Y. Podladchikov (2014), Effects of lithosphere buckling on subsidence and hydrocarbon maturation: A case-study from the ultra-deep East Barents Sea basin, *Earth Planet. Sci. Lett.*, *407*, 123–133.
Goes, S., R. Govers, and P. Vacher (2000), Shallow mantle temperatures under Europe from *P* and *S* wave tomography, *J. Geophys. Res.*, *105*, 11,153–11,169, doi:10.1029/1999JB900300.
Griffin, W. L., S. Y. O'Reilly, N. Abe, S. Aulback, R. M. Davies, N. J. Pearson, B. J. Doyle, and K. Kivi (2003), The origin and evolution of Archean lithospheric mantle, *Precambrian Res.*, *127*, 19–41.
Hackney, R. I., and W. E. Featherstone (2003), Geodetic versus geophysical perspectives of the 'gravity anomaly', *Geophys. J. Int.*, *154*(1), 35–43.
Hansen, S. E., A. J. Rodgers, S. Y. Schwartz, and A. M. Al-Amri (2007), Imaging ruptured lithosphere beneath the Red Sea and Arabian Peninsula, *Earth Planet. Sci. Lett.*, *259*(3), 256–265.
Kaban, M. K., and V. Trubitsyn (2012), Density structure of the mantle transition zone and the dynamic geoid, *J. Geodyn.*, *59-60*, 183–192.
Kaban, M. K., and T. R. Yuanda (2014), Density structure, isostatic balance and tectonic models of the Central Tien Shan, *Surv. Geophys.*, *35*, 1375–1391, doi:10.1007/s10712-014-9298-7.
Kaban, M. K., P. Schwintzer, and C. Reigber (2004), A new isostatic model of the lithosphere and gravity field, *J. Geod.*, *78*, 368–385.
Kaban, M. K., M. Tesauro, and S. Cloetingh (2010), An integrated gravity model for Europe's crust and upper mantle, *Earth Planet. Sci. Lett.*, doi:10.1016/j.epsl.2010.04.041.
Kaban, M. K., A. G. Petrunin, H. Schmeling, and M. Shahraki (2014), Effect of decoupling of lithospheric plates on the observed geoid, *Surv. Geophys.*, *35*, 1361–1373, doi:10.1007/s10712-014-9281-3.
Kaban, M. K., W. D. Mooney, and A. G. Petrunin (2015a), Cratonic root beneath North America shifted by basal drag from the convecting mantle, *Nat. Geosci.*, doi:10.1038/ngeo2525.
Kaban, M. K., S. El Khrepy, and N. Al-Arifi (2015b), Isostatic model and isostatic gravity anomalies of the Arabian plate and surroundings, *Pure Appl. Geophys.*, *173*, 1211–1221, doi:10.1007/s00024-015-1164-0.
Korostelev, F., et al. (2014), Crustal and upper mantle structure beneath south-western margin of the Arabian Peninsula from teleseismic tomography, *Geochem. Geophys. Geosyst.*, *15*, 2850–2864, doi:10.1002/2014GC005316.
Laske, G., G. Masters, Z. Ma, and M. Pasyanos (2013), Update on CRUST1.0—A 1-degree global model of Earth's crust, *Geophys. Res. Abstr.*, *15*, Abstract EGU2013-2658.
Lee, C.-T. (2003), Compositional variation of density and seismic velocities in natural peridotites at STP conditions: Implications for seismic imaging of compositional heterogeneities in the upper mantle, *J. Geophys. Res.*, *108*(B9), 2441, doi:10.1029/2003JB002413.
McDonough, W. F., and S.-S. Sun (1995), The composition of the Earth, *Chem. Geol.*, *120*, 223–253.
Mooney, W. D. (2007), Crust and lithospheric structure—Global crustal structure, in *Treatise on Geophysics*, vol. 1, edited by B. Romanowicz, A. Dziewonski, and G. Schubert, Chap. 11, pp. 361–417, Elsevier, Amsterdam.
Mooney, W. D., and M. K. Kaban (2010), The North American upper mantle: Density, composition, and evolution, *J. Geophys. Res.*, *115*, B12424, doi:10.1029/2010JB000866.
O'Reilly, S. Y., and W. L. Griffin (2012), Mantle metasomatism, in *Metasomatism and the Chemical Transformation of Rock*, *Lect. Notes in Earth Syst. Sci.*, edited by D. E. Harlov, and H. Austrheim, pp. 467–528, Springer, Berlin, doi:10.1007/978-3-642-28394-9_12.
Papazachos, B. C., V. G. Karakostas, C. B. Papazachos, and E. M. Scordilis (2000), The geometry of the Wadati–Benioff zone and lithospheric kinematics in the Hellenic arc, *Tectonophysics*, *319*(4), 275–300.
Petrunin, A. G., I. Rogozhina, A. P. M. Vaughan, I. T. Kukkonen, M. K. Kaban, I. Koulakov, and M. Thomas (2013), Heat flux variations beneath central Greenland's ice due to anomalously thin lithosphere, *Nat. Geosci.*, *6*, 746–750.
Polatidis, A., A. Kiratzi, P. Hatzidimitriou, and B. Margaris (2003), Attenuation of shear-waves in the back-arc region of the Hellenic arc for frequencies from 0.6 to 16 Hz, *Tectonophysics*, *367*(1), 29–40.

Priestley, K., D. McKenzie, J. Barron, M. Tatar, and E. Debayle (2012), The Zagros core: Deformation of the continental lithospheric mantle, *Geochem. Geophys. Geosyst.*, *13*, Q11014, doi:10.1029/2012GC004435.

Schaeffer, A. J., and S. Lebedev (2013), Global shear-speed structure of the upper mantle and transition zone, *Geophys. J. Int.*, *194*(1), 417–449.

Seber, D., E. Sandvol, C. Sandvol, C. Brindisi, and M. Barazangi (2001), Crustal model for the Middle East and North Africa region: Implications for the isostatic compensation mechanism, *Geophys. J. Int.*, *147*, 630–638.

Smit, J., J. P. Brun, S. Cloetingh, and Z. Ben-Avraham (2010), The rift-like structure and asymmetry of the Dead Sea fault, *Earth Planet. Sci. Lett.*, *290*, 74–82, doi:10.1016/j.epsl.2009.11.060.

Steinberger, B., and A. R. Calderwood (2006), Models of large-scale viscous flow in the Earth's mantle with constraints from mineral physics and surface observations, *Geophys. J. Int.*, *167*, 1461–1481.

Stern, R. J., and P. Johnson (2010), Continental lithosphere of the Arabian Plate: A geologic, petrologic, and geophysical synthesis, *Earth Sci. Rev.*, *101*, 29–67.

Stixrude, L., and C. Lithgow-Bertelloni (2005), Thermodynamics of mantle minerals—I. Physical properties, *Geophys. J. Int.*, *162*, 610–632.

Stolk, W., M. K. Kaban, F. Beekman, M. Tesauro, W. D. Mooney, and S. Cloetingh (2013), High resolution regional crustal models from irregularly distributed data: Application to Asia and adjacent areas, *Tectonophysics*, *602*, 55–68.

Storchak, D. A., D. Di Giacomo, I. Bondár, E. R. Engdahl, J. Harris, W. H. K. Lee, A. Villaseñor, and P. Bormann (2013), Public release of the ISC-GEM global instrumental earthquake catalogue (1900–2009), *Seismol. Res. Lett.*, *84*(5), 810–815, doi:10.1785/0220130034.

Tesauro, M., M. K. Kaban, and S. A. P. L. Cloetingh (2008), EuCRUST-07: A new reference model for the European crust, *Geophys. Res. Lett.*, *35*, L05313, doi:10.1029/2007GL032244.

Tesauro, M., M. K. Kaban, W. D. Mooney, and S. A. P. L. Cloetingh (2014), Density, temperature and composition of the North American lithosphere: New insights form a joint analysis of seismic, gravity and mineral physics data. Part II: Thermal and compositional model of the upper mantle, *Geochem. Geophys. Geosyst.*, *15*, 4781–4807, doi:10.1002/2014GC005484.

Wilson, J. W. P., G. G. Roberts, M. J. Hoggard, and N. J. White (2014), Cenozoic epeirogeny of the Arabian Peninsula from drainage modeling, *Geochem. Geophys. Geosyst.*, *15*, 3723–3761, doi:10.1002/2014GC005283.

Yegorova, T. P., V. I. Starostenko, V. G. Kozlenko, and J. Yliniemi (2004), Lithosphere structure of the Ukrainian shield and pripyat trough in the region of EUROBRIDGE-97 (Ukraine and Belarus) from gravity modelling, *Tectonophysics*, *381*(1), 29–59.